The Astronomical Journal, 155:216 (13pp), 2018 May https://doi.org/10.3847/1538-3881/aab902

Phase-dependent Photometric and Spectroscopic Characterization of the MASTER-Net Optical Transient J212444.87+321738.3: An Oxygen-rich Mira

Supriyo Ghosh[1], Soumen Mondal[1], Ramkrishna Das[1], D. P. K. Banerjee[2], N. M. Ashok[2], Franz-Josef Hambsch[3,4], and Somnath Dutta[1]

[1] S. N. Bose National Centre for Basic Sciences, Salt Lake, Kolkata-700 106, India; supriyo12a@boson.bose.res.in, soumen.mondal@bose.res.in
[2] Physical Research Laboratory, Navrangpura, Ahmedabad-380 009, India
[3] Vereniging Voor Sterrenkunde (VVS), Brugge, B-8000, Belgium
[4] American Association of Variable Star Observers (AAVSO), Cambridge, USA

Received 2017 October 11; revised 2018 March 20; accepted 2018 March 20; published 2018 April 27

Abstract

We describe the time-dependent properties of a new spectroscopically confirmed Mira variable, which was discovered in 2013 as MASTER-Net Optical Transient J212444.87+321738.3 toward the Cygnus constellation. We have performed long-term optical/near-infrared (NIR) photometric and spectroscopic observations to characterize the object. From the optical/NIR light curves, we estimate a variability period of 465 ± 30 days. The wavelength-dependent amplitudes of the observed light curves range from $\Delta I \sim 4$ mag to $\Delta K \sim 1.5$ mag. The $(J-K)$ color index varies from 1.78 to 2.62 mag over phases. Interestingly, a phase lag of ∼60 days between optical and NIR light curves is also seen, as in other Miras. Our optical/NIR spectra show molecular features of TiO, VO, CO, and strong water bands that are a typical signature of oxygen-rich Mira. We rule out S- or C-type as ZrO bands at 1.03 and 1.06 μm and C_2 band at 1.77 μm are absent. We estimate the effective temperature of the object from the Spectral Energy Distribution, and distance and luminosity from standard Period–Luminosity relations. The optical/NIR spectra display time-dependent atomic and molecular features (e.g., TiO, Na I, Ca I, H_2O, CO), as commonly observed in Miras. Such spectroscopic observations are useful for studying pulsation variability in Miras.

Key words: infrared: stars – methods: observational – stars: AGB and post-AGB – stars: late-type – stars: variables: general – techniques: spectroscopic

Supporting material: data behind figures

1. Introduction

Mira-type variables are in the Asymptotic giant branch (AGB) phase, which is the last stage of stellar evolution before they turn into planetary nebulae. Miras are long-period (100–1000 days) pulsating variables with a large visible amplitude of more than 2.5 mag. These giants have initial masses ≈0.8–8 $M_\odot$ (low to intermediate main-sequence mass) and are generally surrounded by circumstellar matter from huge mass-loss rates of $\sim 10^{-8}$–$10^{-4}\,M_\odot\,\mathrm{yr}^{-1}$ (Jura & Kleinmann 1990; Habing 1996; Mattei 1997; Olofsson 2004; Herwig 2005). Mira variables have a low effective temperature (<3500 K), cool extended atmospheres (radius up to few 100 $R_\odot$), and luminosities that can reach up to several $10^3\,L_\odot$ (Mattei 1997). High luminous Mira variables play a significant role in the studies of stellar evolution, stellar populations, and galactic/extragalactic structure and evolution (Dejonghe & van Caelenberg 1999; Lançon et al. 1999; Groenewegen et al. 2009), and they enrich the interstellar medium significantly through their high mass loss (Habing 1996). The high mass loss and relatively low surface temperature of these evolved stars provide a habitable zone for several molecules such as TiO, VO, H_2O, and CO in their extended atmospheres. These molecules play important roles in the spectral appearance of Mira variable stars at visual and NIR wavelengths (Lançon & Wood 2000; Gautschy-Loidl et al. 2004; Aringer et al. 2009; Nowotny et al. 2010).

The stars in the AGB phase are radially pulsating and become unstable. Mira variables are thought to be fundamental mode pulsators (e.g., Wood et al. 1999; Ita et al. 2004). The pulsation mode of Miras is a function of period, mass, and radius (Wood & Sebo 1996). The Mira pulsation is thought to originate from the variable ionization zone of hydrogen and helium below the stellar surface (e.g., Keeley 1970). From each pulsation cycle, shock waves are generated under the photospheric surface, which in turn create a very complex and dynamic atmosphere (Reid & Goldston 2002). The photometric light curves of Mira variables represent the oscillating behavior of brightness, surface temperature, radius, atmospheric structure, and opacity as the star pulsates (Le Bertre 1992; Castelaz et al. 2000). The significant visual variation is attributed to the opacity variation of metal oxides in the Mira atmosphere (Reid & Goldston 2002). The observed radii of Mira stars significantly differ at different optical/NIR wavelengths as seen from high angular resolution observations (e.g., Thompson et al. 2002; Ireland et al. 2004; Perrin et al. 2004; Mondal & Chandrasekhar 2005). These results indicate the presence of molecular layers above the continuum-forming photosphere (Wittkowski et al. 2008). The theoretical hydrodynamic pulsation models have been developed to understand the pulsation and mass-loss mechanisms, which can predict the time-dependent structure and temporal variations over multiple cycles (Fleischer et al. 1992; Bessell et al. 1996; Winters et al. 1997, 2000; Höfner et al. 1998; Loidl et al. 1999; Tej et al. 2003b). These models are characterized by pulsation-driven shocks, non-equilibrium chemistry, and the formation of dust grains (Bieging et al. 2002).

Spectroscopic observational studies are valuable tools to understand pulsating atmospheres and mass loss of Mira

variables throughout the outer layer (Hinkle et al. 1982; Castelaz & Luttermoser 1997; Alvarez et al. 2000; Castelaz et al. 2000; Lançon & Wood 2000; Tej et al. 2003a). Phase-dependent spectroscopic studies are very efficient for probing the atmospheres of the stars, and such studies are limited in the literature. From radial velocity, excitation temperatures and line-broadening measurements using high-resolution spectroscopy, it is evident that two separate line-forming regions of the atmosphere sometimes contribute toward the spectrum of H_2O (except maximum light), CO ($\Delta\nu = 2$) and OH (Hinkle 1978; Hinkle & Barnes 1979a; Nowotny et al. 2010). More complex stratification may also exist (e.g., Tej et al. 2003b; Tsuji 2009).

In this paper, we have studied an object, which was first detected from Mobile Astronomical System of TElescope Robots (MASTER) Optical Transient (OT) alert on J212444.87+321738.3 (hereafter, J2124+32) on 2013 March 13 with 10.7 mag at unfiltered CCD (Tiurina et al. 2013). The MASTER Global Robotic Net[5] consists of several identical observing instruments at different observatories (e.g., MASTER-Amur, MASTER-Tunka, MASTER-SAAO). The facilities provide very fast sky-survey (128 deg^2 per hour) with limiting magnitude 19–20 (Lipunov et al. 2016, 2017). The primary goals of the MASTER-net are to observe gamma-ray bursts in alert mode. However, it discovers many OTs in the survey mode. The other identification of the object (J2124+32) is USNO-B1.0 1222-0647260, 2MASS 21244500+3217377, and WISE J212444.98+321737.73.440 (Tiurina et al. 2013). Following the OT announcement, we have started spectro-photometric monitoring observations on the object in optical/NIR wavelength since 2013 March 20 for more than 1.5 years using different telescope facilities. We present here the result of the characterization of MASTER OT J2124+32, which turns out to be a new O-rich Mira variable. From the third and fourth edition of General Catalog Variable Stars, the galactic Mira detection limit is complete down to a maximum magnitude $V \approx 9$ mag (Kharchenko et al. 2002). This new Mira variable has a peak magnitude at I-band $\approx$10.4 mag, which corresponds to $V \approx 14$ (Kharchenko et al. 2002). Because of faintness, the object might not be included in the variability monitoring program. This paper is organized as follows. We describe the details of our observations and data reduction procedures in Section 2. Section 3 presents our new results and discussion. Finally, the summary and conclusion of our studies are presented in Section 4.

2. Observations and Data Reduction

Optical imaging observations of J2124+32 were performed using a front-illuminated 4K × 4K CCD camera on the 40 cm $f/6.8$ Optimized Dall Kirkham telescope at the private observatory ROAD (Remote Observatory Atacama Desert) in Chile (Hambsch 2012). The source was monitored in the optical I-band and unfiltered CCD (400–900 nm) filter-band (Clear, C) over 550 days during 2013 April 02 to 2014 August 31. The accuracy of these observations varies from 0.004 at $I = 10.40$ to 0.047 at $I = 14.30$, while from 0.007 at $C = 12.35$ to 0.045 at $C = 15.70$ mag, respectively.

The NIR photometric and spectroscopic observations were carried out using Near-Infrared Imaging Camera cum Multi-Object Spectrograph (NICMOS-3) on 1.2 m Mt. Abu telescope, India, and TIFR Near-Infrared Spectrometer and Imager (TIRSPEC) on 2 m Himalayan *Chandra* Telescope (HCT) at Hanle, India. The NICMOS3 has 256 × 256 HgCdTe detector array and provides a resolution $R \approx 1000$; while TIRSPEC has 1024 × 1024 Hawaii-1 array and provides resolution $R \approx 1200$. The spectral coverage of NICMOS-3 were on *JHK*-bands. The spectrograph in the NICMOS-3 instrument does not cover the whole K-band in a single shot. We observed in two parts: the first part covers 1.9–2.3 μm (termed as K), and the second part covers 2.1–2.4 μm with some overlap (termed as KA). The TIRSPEC spectra were taken at the *YJHK* bands. Additional details of TIRSPEC can be found in Ninan et al. (2014). Photometric observations in JHK'-bands were taken in five dithered positions, and multiple frames are taken in each dithered position to get better signal to noise ratio (S/N). In spectroscopic observing mode, the spectra were taken at two different positions along the slit, one after another, immediately to subtract the sky, and several frames were observed to improve the S/N. We have estimated the S/N of our spectra as ∼50 (J-band), ∼80 (H-band), and ∼80–100 (K-band) for TIRSPEC data, while the S/N is ∼30 (JHK) for the NICMOS-3 data. A log of our observations is mentioned in Table 1.

The optical spectra are taken using Himalaya Faint Object Spectrograph and Camera (HFOSC) on the 2 m HCT at Hanle, India. The HFOSC instrument has several grisms covering different wavelength ranges and resolutions, and we have used Grism No. 8 (Gr#8) for our studies, which covers the wavelength range of 580–920 nm and provides a resolution $R \approx 2200$.[6]

The data reduction was performed with the help of standard tasks of the Image Reduction and Analysis Facility (IRAF[7]). In NIR photometric reduction, the sky frames were generated using all dithered frames by median combining and subtracting from object frames. In optical photometric reduction, bias-correction, flat-fielding, and removal of cosmic rays were performed on raw images to clean the science frames. The aperture photometry was carried out with these processed images using APPHOT package of IRAF. The zero-points of photometry were determined using the standard stars.

The spectroscopic analysis was done using the APALL task of IRAF. The TIRSPEC data was reduced with the TIRSPEC pipe-line[8] (Ninan et al. 2014) and was cross-checked with the IRAF reduction. Both techniques agree well. The wavelength calibration in the NICMOS-3 data was performed using OH skylines, while Argon lamp is used for TIRSPEC data. The wavelength calibration of optical spectra (HFOSC data) was done by using an FeNe arc spectrum. The science frames are divided by a standard star, observed at similar airmasses to the science targets, to remove the telluric features of the Earth's atmosphere. Then, the flux calibration of the target stars is performed using the standard star.

3. Result and Discussion

3.1. Optical Light Curves and Period

Figure 1 shows the optical light curves in the I-band and unfiltered (400–900 nm) CCD (Clear, C). The amplitudes of optical variability are estimated to be ∼4.00 mag and ∼3.4 mag in the I band and unfiltered CCD, respectively. Such large amplitude of variability with a long-term period is only observed in a case of Mira-like variables (Whitelock et al. 2003). The general criteria for being a Mira variable is having amplitude

[5] http://observ.pereplet.ru/

[6] https://www.iiap.res.in/iao_hfosc

[7] http://iraf.noao.edu/

[8] https://github.com/indiajoe/TIRSPEC/wiki

Table 1
Log of Photometric and Spectroscopic Observations

Date of Observation	Observation Type	Spectral Band	Int. Time (s)	No of Frames	Telescope	Remarks
2013 Mar 20	Photometry	*J/H/K*	0.4/0.2/0.2	5* [21/21/21]	1.2 m Mt. Abu	clear sky
2013 Mar 22	Photometry	*J/H/K*	0.5/0.4/0.2	5* [11/11/21]	1.2 m Mt. Abu	clear sky
2013 Apr 28	Photometry	*J/H/K*	2/1/0.3	5* [15/15/25]	1.2 m Mt. Abu	clear sky
2013 Apr 29	Photometry	*J/H/K*	0.5/0.5/0.2	5* [31/31/31]	1.2 m Mt. Abu	clear sky
2013 May 27	Photometry	*J/H/K*	0.3/0.7/1	5* [15/15/35]	1.2 m Mt. Abu	clear sky
2013 May 28	Photometry	*J/H/K*	1/1/0.3	5* [21/21/35]	1.2 m Mt. Abu	clear sky
2013 May 30	Photometry	*J/H/K*	0.3/0.5/1	5* [15/15/15]	1.2 m Mt. Abu	clear sky
2013 Jun 20	Photometry	*J/H/K*	0.3/0.5/1	5* [15/15/15]	1.2 m Mt. Abu	clear sky
2013 Oct 30	Photometry	*J/H/K*	0.3/0.5/1	5* [15/15/15]	1.2 m Mt. Abu	clear sky
2015 May 08	Photometry	*J/H/K*	0.3/0.5/1	5* [15/15/15]	1.2 m Mt. Abu	clear sky
2013 Apr 02 - 2014 Aug 31	Photometry	I/CV	60/30	515/515	40 cm Chile	⋯
2013 Mar 20	Spectroscopy	*J/H/K*/KA	120/90/60/60	2*1	1.2 m Mt. Abu	clear sky
2013 Apr 28	Spectroscopy	*J/H/K*/KA	90/75/60/60	2*1	1.2 m Mt. Abu	clear sky
2013 May 30	Spectroscopy	*J/H/K*/KA	90/60/60/60	2*1	1.2 m Mt. Abu	clear sky
2013 Oct 15	Spectroscopy	600–920 nm	1800	1	2 m HCT	clear sky
2014 May 21	Spectroscopy	600–920 nm	300	1	2 m HCT	clear sky
2014 Aug 18	Spectroscopy	*H/K*	30/30/20/10	2*5	2 m HCT	clear sky
2014 Aug 19	Spectroscopy	600–920 nm	300	1	2 m HCT	clear sky
2014 Oct 06	Spectroscopy	*YJ/HK*	100/100	2*7	2 m HCT	clear sky
		600–920 nm	600	1		
2014 Dec 12	Spectroscopy	*YJ/HK*	100/100	2*7	2 m HCT	clear sky
		600–920 nm	600	1		
2015 Jan 13	Spectroscopy	*YJ/HK*	100/100	2*7	2 m HCT	clear sky
2015 Jan 18	Spectroscopy	600–920 nm	900	1	2 m HCT	clear sky
2015 Jul 05	Spectroscopy	*YJ/HK*	100/100	2*5	2 m HCT	clear sky
		600–920 nm	1	1		
2015 Aug 11	Spectroscopy	*YJ/HK*	100/100	2*5	2 m HCT	clear sky
2016 Dec 19	Spectroscopy	*HK*	100	2*5	2 m HCT	clear sky

variability in the *I*-band greater than 1.0 mag (Soszyński et al. 2012).

For determination of the period of this object, we used the Lomb–Scargle (LS) periodogram (Lomb 1976; Scargle 1982), the algorithm publicly available at the starlink[9] software database. The LS method is used to find out significant periodicity even with unevenly sampled data and verified successfully in several cases to determine periods from such sparse data sets (Mondal et al. 2010). The left bottom panel of Figure 1 shows the periodograms of the light curves determined from the LS method. We found the period to be 512 ± 100 days, and significant uncertainty in period is due to limited time coverage, which does not cover a complete periodic cycle. The period is also verified from PERIOD04[10] (Lenz & Breger 2005), which provides the same result.

As noted in Lebzelter et al. (1999), the classical method for deriving a period using a Fourier analysis-like LS method does not always provide satisfying results for light curves of AGB variables. Alternatively, we have used the Fourier decomposition technique with the fitting of the following function as in Ngeow et al. (2013),

$$m(t) = A_0 + \sum_{\kappa=1}^{N} A_\kappa \sin(\kappa\omega t + \phi_\kappa) \quad (1)$$

where $\omega = 2\pi/P$, P is the period in days, A_κ and ϕ_κ represent the amplitude and phase-shift for κth-order, respectively, and N is the order of the fit. To fit the light curve, we use up to third-order terms. From the χ^2 minimization technique, we find a best-fitted period of 465 ± 30 days on our light curves. The solid black line is the Fourier fit, which is shown in Figure 1 along with observed data in the respective panels. The estimated period of this red object is consistent with those of the red Large Magellanic Cloud (LMC) Miras ($J - K \geqslant 2.08$) having periods of 300−500 days (Ita et al. 2004).

3.2. Near-infrared Light Curves

NIR *JHK′*-bands photometric observations were carried out during 2013 March 20 to 2015 May 09 in a sparse sampling of the Mira cycle, and *JHK′* magnitudes are listed in Table 2. Our *JHK′* magnitudes on the first two epochs are reported immediately at ATEL (Mondal et al. 2013). The NIR *JHK′* light curves are shown in the right panels of Figure 1. For comparison, the optical *I*-band light curve is also overplotted on those NIR light curves after scaling with *JHK′* magnitudes. The light curve is fitted to the Equation (1) mentioned above with the same period of the optical light curve fit. The amplitudes (peak to peak) of the variability are estimated from our light curves to be $\Delta J \sim 2.2$ mag, $\Delta H \sim 1.9$ mag, and $\Delta K \sim 1.5$ mag, respectively. These optical/NIR light curves confirm typical Mira behavior of strong wavelength dependence, i.e., the pulsation amplitude decreases with increasing

[9] http://starlink.eao.hawaii.edu/starlink
[10] http://www.univie.ac.at/tops/Period04

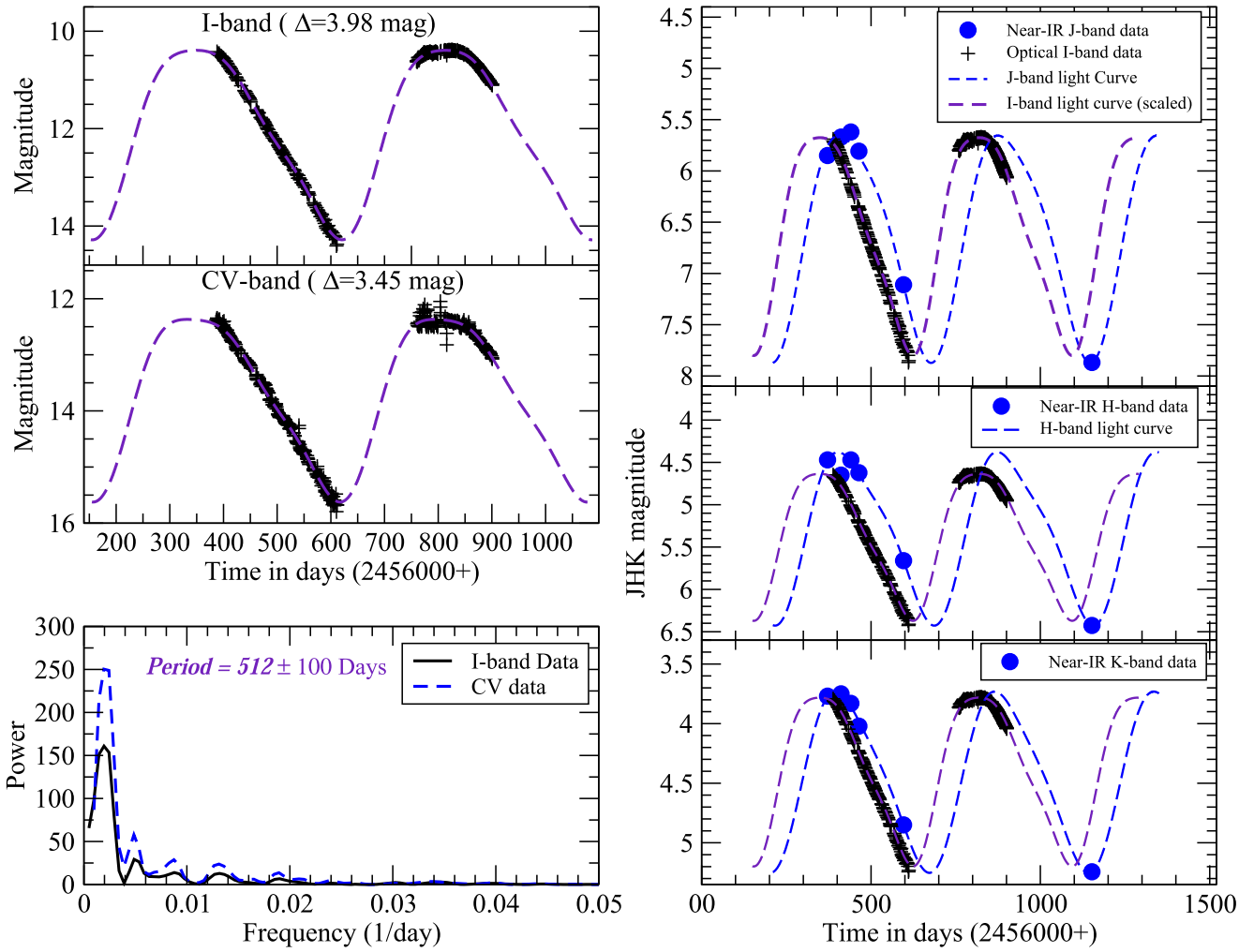

Figure 1. The left panels show the optical light curves of J2124+32 with fitting using Equation (1) in the *I*-band (left top) and unfiltered CCD in 400–900 nm (C) (left middle). The periodograms of optical light curves are shown in the left bottom panel. The NIR *JHK* light curves of J2124+32 are shown in the right three panels (*JHK′*), where the filled circles are our observed NIR data points, while the solid lines are fitted light curves with $P = 465$ days. The optical *I*-band light curve (scaled with NIR light curves) is overplotted on NIR light curves for comparison. The data used to create this figure are available.

Table 2
Near-IR *JHK′* Photometry

Date of Obs. (UT)	Optical Phase	Telescope/Instrument	*J* (mag)	*H* (mag)	*K* (mag)	(*J* − *K*) (mag)
2013 Mar 22.02	0.049	Mt. Abu/NICMOS-3	5.852 ± 0.055	4.467 ± 0.062	3.765 ± 0.049	2.087
2013 Mar 24.01	0.051	Mt. Abu/NICMOS-3	5.642 ± 0.044	4.483 ± 0.035	3.765 ± 0.034	1.877
2013 Apr 28.93	0.118	Mt. Abu/NICMOS-3	5.668 ± 0.043	4.654 ± 0.052	3.751 ± 0.010	1.917
2013 Apr 29.98	0.119	Mt. Abu/NICMOS-3	5.557 ± 0.021	4.510 ± 0.023	3.720 ± 0.012	1.837
2013 May 27.92	0.169	Mt. Abu/NICMOS-3	5.621 ± 0.051	4.466 ± 0.063	3.827 ± 0.045	1.794
2013 May 28.95	0.170	Mt. Abu/NICMOS-3	5.718 ± 0.047	4.452 ± 0.053	3.752 ± 0.048	1.966
2013 Jun 20.83	0.213	Mt. Abu/NICMOS-3	5.807 ± 0.034	4.621 ± 0.024	4.021 ± 0.029	1.786
2013 Oct 30.50	0.450	Mt. Abu/NICMOS-3	7.110 ± 0.020	5.660 ± 0.030	4.850 ± 0.020	2.260
2015 May 08.91	1.60	Mt. Abu/NICMOS-3	7.868 ± 0.017	6.426 ± 0.06	5.243 ± 0.015	2.625
1998 Jun 18.00[a]		2MASS/NICMOS	7.825 ± 0.026	5.971 ± 0.017	4.818 ± 0.015	3.007
Average		Mt. Abu/NICMOS3	6.093 ± 0.257	4.859 ± 0.220	4.077 ± 0.17	2.016
Amplitude (light curve)		Mt. Abu/NICMOS3	2.2	1.9	1.5	

Note.
[a] Cutri et al. (2003).

wavelength (Smith et al. 2002). Bessell et al. (1996) showed that colors such as $V-K$ change much more with phase than near-IR colors (e.g., $(J-H)$, $(H-K)$, $(J-K)$), which is another way of saying that visual amplitudes are larger than near-IR amplitudes. The fact that the pulsation amplitude decreases with increasing wavelength is a result of the changes in $T_{\rm eff}$ that accompany the changes in luminosity, which is exacerbated by the dependence of TiO opacities on temperature. Another interesting feature, a phase lag of about 60 days, corresponding to ~0.13 of phase, between the optical and NIR maxima or minima is observed here in Figure 1, which is seen in Mira variables (Smith et al. 2002). Such phase lag in oxygen-rich Miras may be due to the opacity of TiO molecules in their atmosphere (Smith et al. 2006), and even large visual amplitudes might be due to the formation and destruction of TiO molecules during the passage of periodic shock waves (Reid & Goldston 2002). The 2MASS $(J-K)$ color is 3.0 mag (Cutri et al. 2003). We also find a large $(J-K)$ color index, ranging from 1.78 to 3.0 mag (Table 2), which is, again, consistent with the source being an extreme red Mira variable (Whitelock et al. 2000; Ita et al. 2004). We rule out that the object is a semi-regular variable, as they are not this degree of red.

3.3. Distances and Luminosity

To estimate the distance to the source, we have used the period−luminosity (PL) relation for the Miras based on the distance modulus of the LMC to be 18.50 ± 0.02. The PL relation is taken from Ita & Matsunaga (2011) expressed as

$$M_K = (-3.675 \pm 0.076)\log P + (1.456 \pm 0.173). \quad (2)$$

According to the relation, the absolute K-band magnitude of the source is estimated to be $M_K = -8.34 \pm 0.34$ mag. We have also examined other available PL relations in Feast et al. (1989) and Whitelock et al. (2008), and the value of M_K is within the uncertainty limit. The Galactic interstellar extinction in the direction of the source is $A_V = 0.57$ ($A_K = 0.05$; Schlafly & Finkbeiner 2011) or $A_V = 0.68$ ($A_K = 0.06$; Schlegel et al. 1998). Taking $A_K = 0.05$, we have obtained the distance, d, to the object, 3.27 ± 0.02 kpc using the relation $m_k - M_K = 5\log d - 5 + A_K$. The uncertainties in the distance measurement come from the estimated period, PL relation, and photometric error of calculating the K-band magnitude. We have also estimated the bolometric magnitude $M_{\rm bol}$ using the following PL relation for Miras (Hughes & Wood 1990)

$$M_{\rm bol} = -3.22–7.76[\log(P/\text{day}) - 2.4] \pm 0.38. \quad (3)$$

We have estimated the bolometric magnitude of $M_{\rm bol} = -5.29 \pm 0.38$ corresponding to luminosity ~10250 $L_\odot$, which is consistent with other PL relation of Feast et al. (1989). The O-rich Miras with $P \geqslant 420$ days are over luminous (Feast et al. 1989; Hughes & Wood 1990), which is consistent with our result. Feast et al. (1989) showed that a few Miras, which have periods >420 days, are 0.7 mag brighter than the expected extrapolation of the PL relation. Also, Whitelock et al. (2003) suggested that Miras' with periods >400 days have higher luminosities due to hot bottom burning. Puttingour object on the mass–luminosity relation in Figure 6 of Hughes & Wood (1990), the object with $P = 465$ days and $M_{\rm bol} = -5.29$ lies between the mass (M) range of $1.0\,M_\odot - 1.5\,M_\odot$.

To understand the galactic location of the new Mira variable, we have estimated the scale height of the object from the distance above the galactic plane (Z) following Jura & Kleinmann (1992). We find that the scale height of the object is about 270 pc, which agrees with the thin disk population as given by Habing (1988), Jura & Kleinmann (1992), Eggen (1998), and Jurić et al. (2008).

3.4. Spectral Energy Distribution (SED)

We use near to far-infrared multi-wavelength photometric data to generate the SED of the source J2124+32. The fluxes, used here for the SED fit, are taken from our *JHK′* measurements and archival mid- to far-infrared catalogs. The mean *JHK′* are estimated from the NIR light curves. The mid-IR 3.35, 11.6, and 22.1 μm data are taken from AllWISE Data Release (Cutri et al. 2013); 8.61, 18.4 μm from *AKARI*/IRC all-sky Survey (ISAS/JAXA, 2010; Ishihara et al. 2010); 12, 25 μm from *IRAS* Faint Source Catalog (IPAC 1992) and Far-IR 65, 90 μm data from *AKARI*/FIS; and 60 μm from *IRAS*. The observed *JHK′* magnitudes are converted to flux densities using the zero magnitudes flux from Bessell et al. (1998).

The radiative transfer code, More of Dusty[11] (MoD), developed by (Groenewegen 2012), was used to model the dusty circumstellar shell of Mira variable. The MoD is a modified version of a publicly available one-dimensional dust radiative transfer code, "DUSTY" version 2.01 (Ivezić & Elitzur 1999). The detail mathematical formulation of "DUSTY" was described elsewhere (Ivezić & Elitzur 1997). The MoD works to find best-fitted parameters, e.g., luminosity (L), dust optical depth ($\tau_{0.55}$), dust temperature at the inner radius (T_c), and slope of the density law (p), in the minimization process. The quality of the fit is obtained through a χ^2 analysis.

The interstellar reddening (A_V), hydrostatic model atmosphere, the effective temperature of the model atmosphere, distance (D), outer radius in a unit of inner radius, dust properties, etc. are provided as inputs in the master-input file. The adopted dust species are taken as mixture of $Mg_{0.8}Fe_{1.2}SiO_4$:AlO:Fe = 100:0:5, calculated using the distribution of hollow spheres (DHS) with a mean grain size $a = 0.15$ μm and a maximum volume fraction of a vacuum core $f_{\rm max} = 0.7$ μm (M. A. T. Groenewegen 2018, private communication). We adopted such dust composition because our spectroscopic studies concluded that the star is O-rich, as will be discussed in subsequent sections. The MARCS[12] hydrostatic model atmospheres (Gustafsson et al. 2008) were used for the spectra of the central stars. The outer radius is set to 1600 times the inner radius, where the dust temperature becomes approximately 20 K. In the model, the distance, d, of 3.27 kpc and A_V were adopted as an inputs to the standard model as discussed in the previous section. The L, τ, T_c, and p could be fitted or set to fixed values.

To obtain the best fit of the photometric data, we generated multiple SEDs considering MARCS model atmospheres of temperature range 2600–3600 K in steps of 200 K and setting other free parameters (e.g., L, $\tau_{0.55}$, T_c, p) as either fixed or variable, as listed in Table 3. This model provides minimum reduced χ^2 value at MARCS model atmospheres of temperature 2800 K, and the parameters of MoD fitting at that temperature for different cases are given in Table 3. Our best-fit SEDs for all photometric measurements for various cases are

[11] http://homepage.oma.be/marting/codes.html
[12] http://marcs.astro.uu.se/

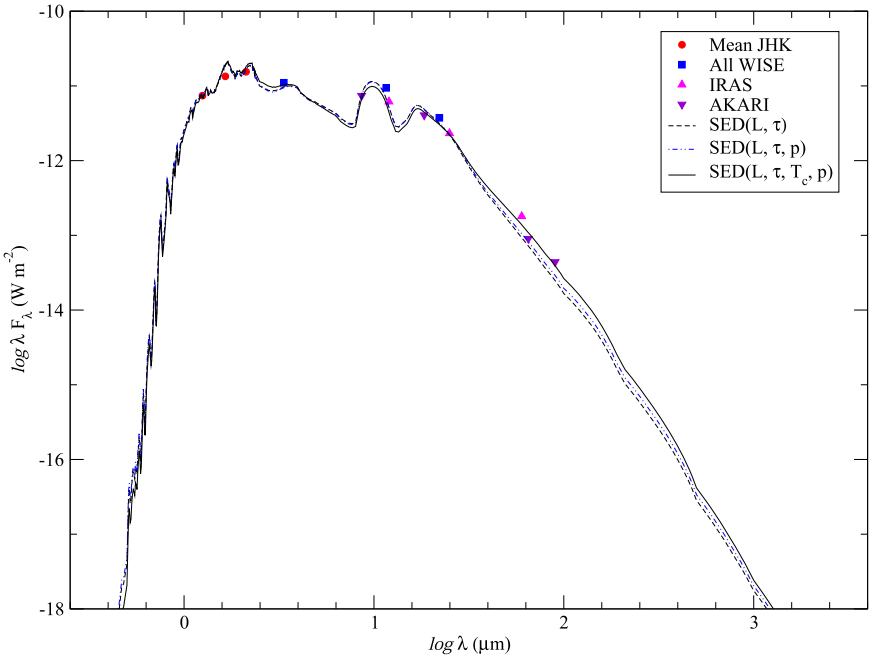

Figure 2. The SED of the target is shown here using multi-wavelength data from NIR to far-IR, while the insets show different data sources, e.g., our mean *JHK′*, All *WISE, AKARI*, and *IRAS* data. The SED (L, τ) mean fitted SED is shown, with L, τ as variables and T_c, p fixed. The same is true for SED (L, τ, p) and SED (L, τ, T_c, p).

Table 3
MoD Models for J2124+32 for Three Different Cases

Star	L ($L\odot$)	$\tau_{0.55}$	T_c (K)	p	$\chi^2_{\rm red}$ [a]	Remarks
	9331 ± 1545	10.064 ± 2.489	1000 fixed	2.0 fixed	819	T_c, p fixed
J2124+32	9255 ± 1659	9.913 ± 2.746	1000 fixed	1.95 ± 0.29	818	T_c fixed
	9282 ± 1590	11.178 ± 3.975	1248 ± 511	1.75 ± 0.28	806	All free

Note.
[a] $\chi^2_{\rm red}$ = reduced χ^2 for the fit of photometric data.

shown in Figure 2. We obtained the minimum value of reduced χ^2 when all of the parameters were set free. The χ^2 of the fit is typically large as we include significant *JHK′* variability in our SED fit and non-simultaneous taking of the photometric data. The provided errors are therefore internal errors scaled to a reduced χ^2 of 1 (M. A. T. Groenewegen 2018, private communication). The best-fitted SED provides $L = 9282 \pm 1590\ L_\odot$ that is comparable to our P-L based estimation in the earlier section, $\tau = 11.178 \pm 3.975$, $T_c = 1248 \pm 511$ K, and $p = 1.75 \pm 0.28$. The best-fit parameters, dust properties, and actual grain size translate into a current mass-loss rate of $0.7 \times 10^{-6}\ M_\odot\ {\rm yr}^{-1}$ by assuming a dust-to-gas ratio of 0.005 and an expansion velocity of 10 km s^{-1}.

3.5. Optical/NIR Spectroscopic Studies

Multi-epoch optical/NIR spectroscopic studies on Mira variables at different variability phases probe the dynamic stellar atmosphere and help us also to understand the pulsational related variations of fundamental parameters. The visual spectra of the object taken at several variability phases are shown in Figure 3. The optical spectra are dominated by molecular absorption bands of TiO and VO in the wavelength range of 7000–9000 Å , like red M stars (Bessell et al. 1989; Fluks et al. 1994; Castelaz et al. 2000; Rayner et al. 2009). A visual comparison shows that all of the optical spectra of the MASTER OT object correspond to O-rich spectral types later than M7.

The NIR spectra were taken immediately after transient alert of Tiurina et al. (2013) and continued over several variability phases as listed in Table 1. The *JHK* spectra are shown in Figure 4. Molecular features of the TiO and VO bands dominate in the *J*-band spectra, as shown in the first panel of Figure 4. But no ZrO twin features at 1.03, and 1.06 μm is seen here, which is a primary indicator for S-type Mira stars (Hinkle et al. 1989; Wright et al. 2009). The most prominent feature of the VO band is seen in one of our spectra, which covers from 1.02 μm, which signifies that it is an oxygen-rich M-type star (Wright et al. 2009).

In the second panel of Figure 4, the *H*-band spectra show the ^{12}CO-second overtone series at 1.5582, 1.5780, 1.5982, 1.6189, 1.6397, 1.6610, 1.6840, and 1.7067 μm including OH molecular bands all over the band (Rayner et al. 2009). These second overtone series develop at objects having photospheric temperatures of $\leqslant$5000 K, and their strength is dependent on the photospheric temperatures (Lançon et al. 2007). The OH molecular bands are prominent in M-type

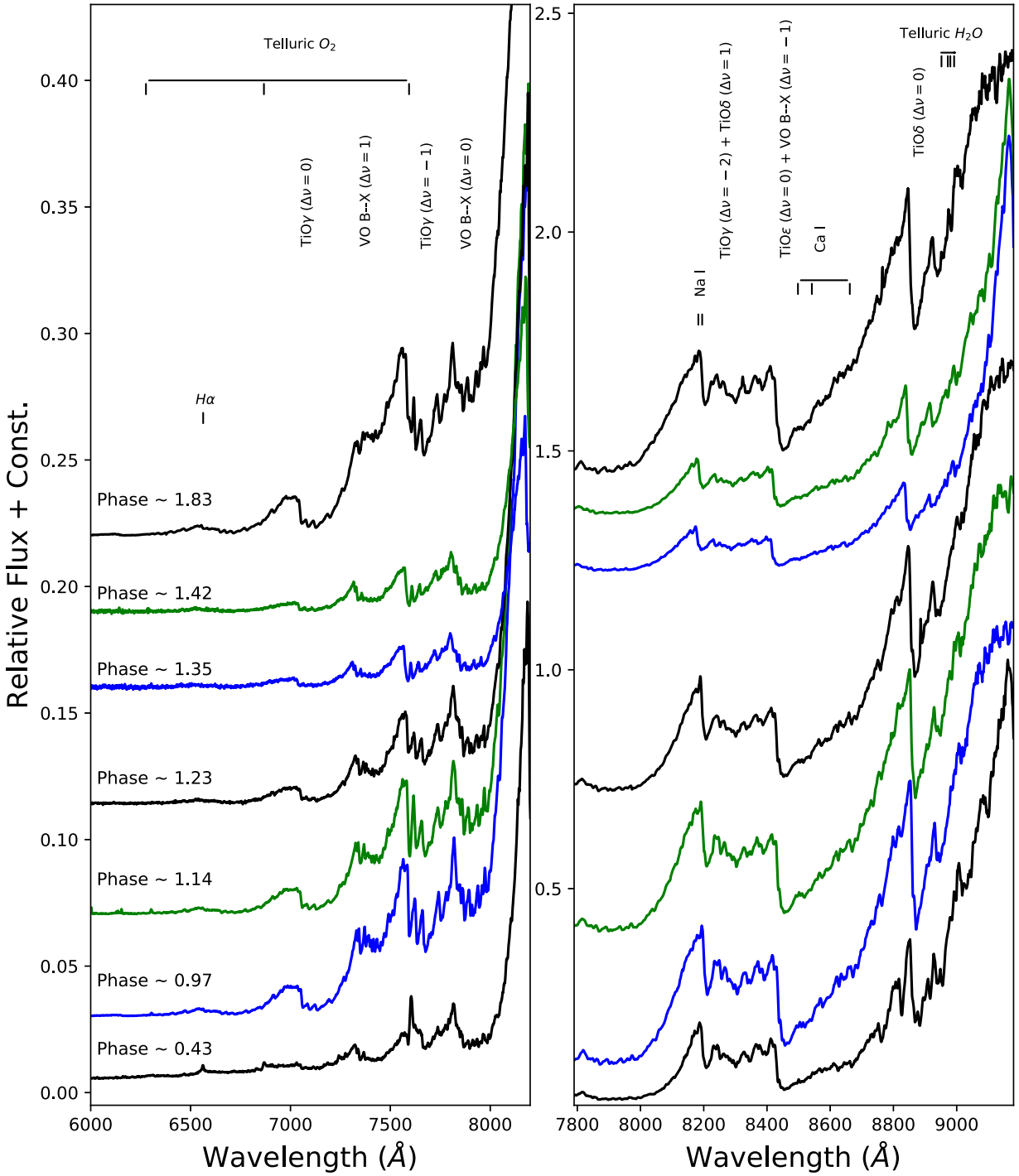

Figure 3. The top two panels show the optical spectra of the object in the range 6000–9200 Å, in which visible features of TiO and VO bands at different phases of the Mira can be clearly seen, including H_α emission at phase 0.43. The spectra have been normalized to unity at 9165 Å and offset by constant values 0.0, 0.03, 0.07, 0.11, 0.16, 0.19, and 0.22 (left panel) and 0.0, 0.06, 0.36, 0.70, 1.20, 1.35, and 1.40 (right panel), respectively, with respect to the bottom-most spectra. The data used to create this figure are available.

stars, very weak in S-type, and absent in carbon stars, as all oxygen is locked up in CO. No C_2 band at 1.77 μm is seen here, as is observed in carbon-rich Miras.

The *K*-band spectra are shown in the most bottom panel of Figure 4. The ^{12}CO first overtone series at 2.2935, 2.3227 μm, neutral atomic lines of Na I doublet at 2.20 μm, Ca I triplet at 2.26 μm are seen in our spectra, which are original features in M-type evolved stars (Rayner et al. 2009). The ^{12}CO(2, 0) first overtone band heads are the strongest absorption features in the *K* band in cool stars, and their strength depends on both luminosity and effective temperature (Ramirez et al. 1997; Cesetti et al. 2013). The first overtone of ^{13}CO is also visible in our spectra, though its strength is relatively weak compared to ^{12}CO first overtone series.

The Hα emission line is seen only at phase ~0.43. The Paβ emission line appears in two visual phases, 1.83 and 1.92. The

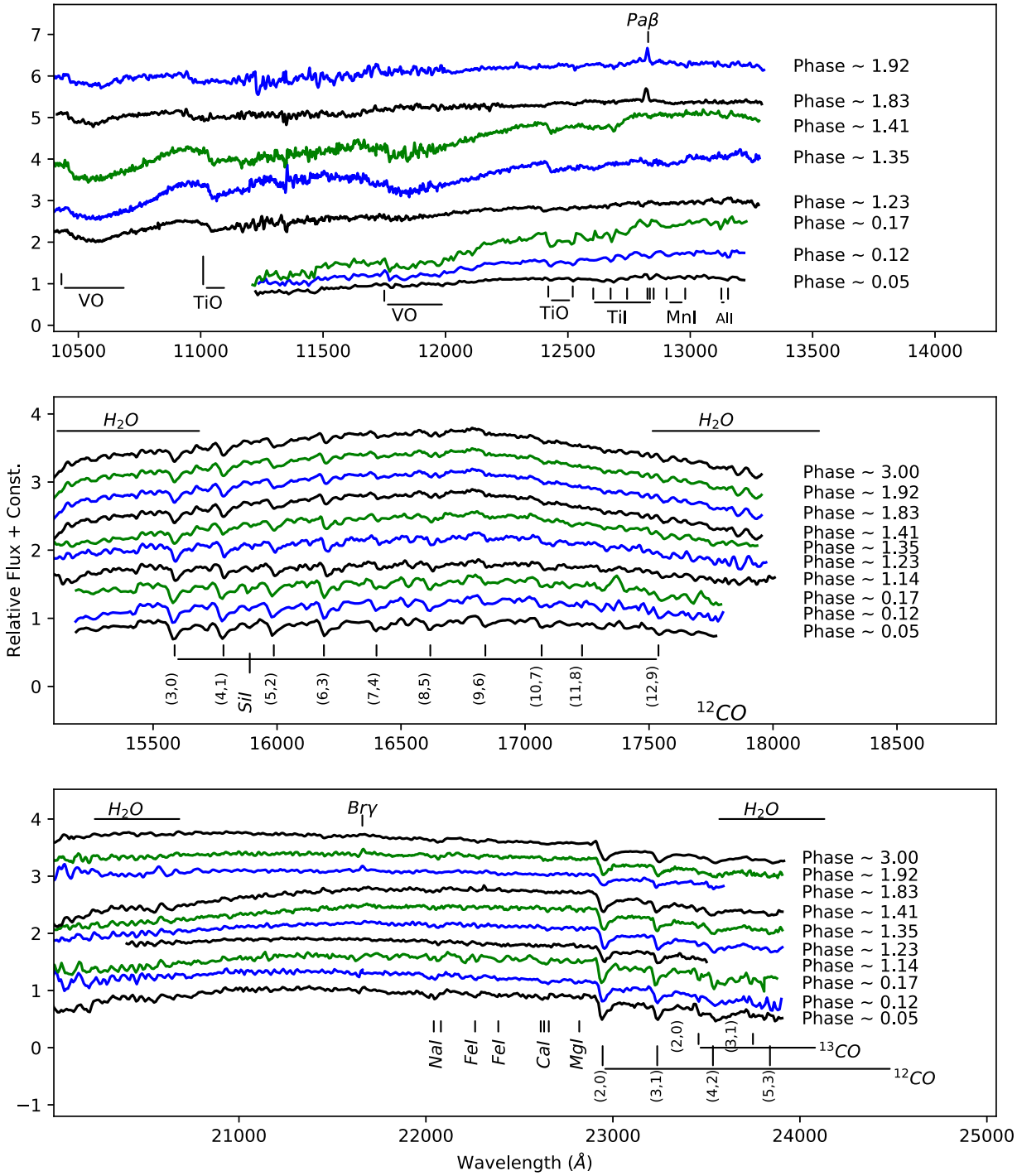

Figure 4. The NIR *JHK*-band spectra in the wavelength range 1.02−2.39 μm at eight different phases of the Mira are shown here in the first, second, and third panels, respectively. The first three NIR spectra from the bottom (phase ∼0.05, 0.12, 0.17) are taken with the NICMOS-3 instrument on 1.2 m Mt.Abu telescope, and rest are observed with TIRSPEC instrument on 2.0 m HCT. In the *J*-band, molecular bands like TiO, VO, and a few atomic lines are present in the spectra. The Paβ emission line appears at two phases (1.83 and 1.92). The *H*-band spectra in the wavelength range 1.52−1.80 μm show strong four ^{12}CO-second overtone bands including several OH lines. In the *K*-band spectra, the ^{12}CO first overtone bands are dominated features in the spectra, and Na I and Ca I are seen at 2.20 μm and 2.26 μm, respectively. The Brγ (at 2.16 μm) emission line appears at phases 1.83, 1.92, and likely at 0.05. The spectra have been normalized to unity at 12000 Å (*J*-band), 16500 Å (*H*-band), and 21700 Å (*K*-band), and offset by constant values 0.0, 0.30, 0.60, 0.11, 1.70, 2.40, 3.30, 4.20, and 5.10 (first panel), respectively, with respect to the bottom-most spectra of the same panel (*J*-band), and 0.30 to each spectrum of the *H*- and *K*-band. The data used to create this figure are available.

Brγ appears at phase 1.83 and reaches maximum intensity at 1.92. These emission lines appear in the spectra due to shock wave generation in the Mira atmosphere. It should be noted that Hα is seen at phase 0.43, while Paβ and Brγ are seen near the maximum phase. Other studies find Balmer lines usually around the maximum phase (e.g., Fox et al. 1984; Fox & Wood 1985).

The overall low-resolution continuum shape of *J, H*, and *K* spectra turns downwards at the end of the band, indicating absorption due to broad H_2O absorption features centered at

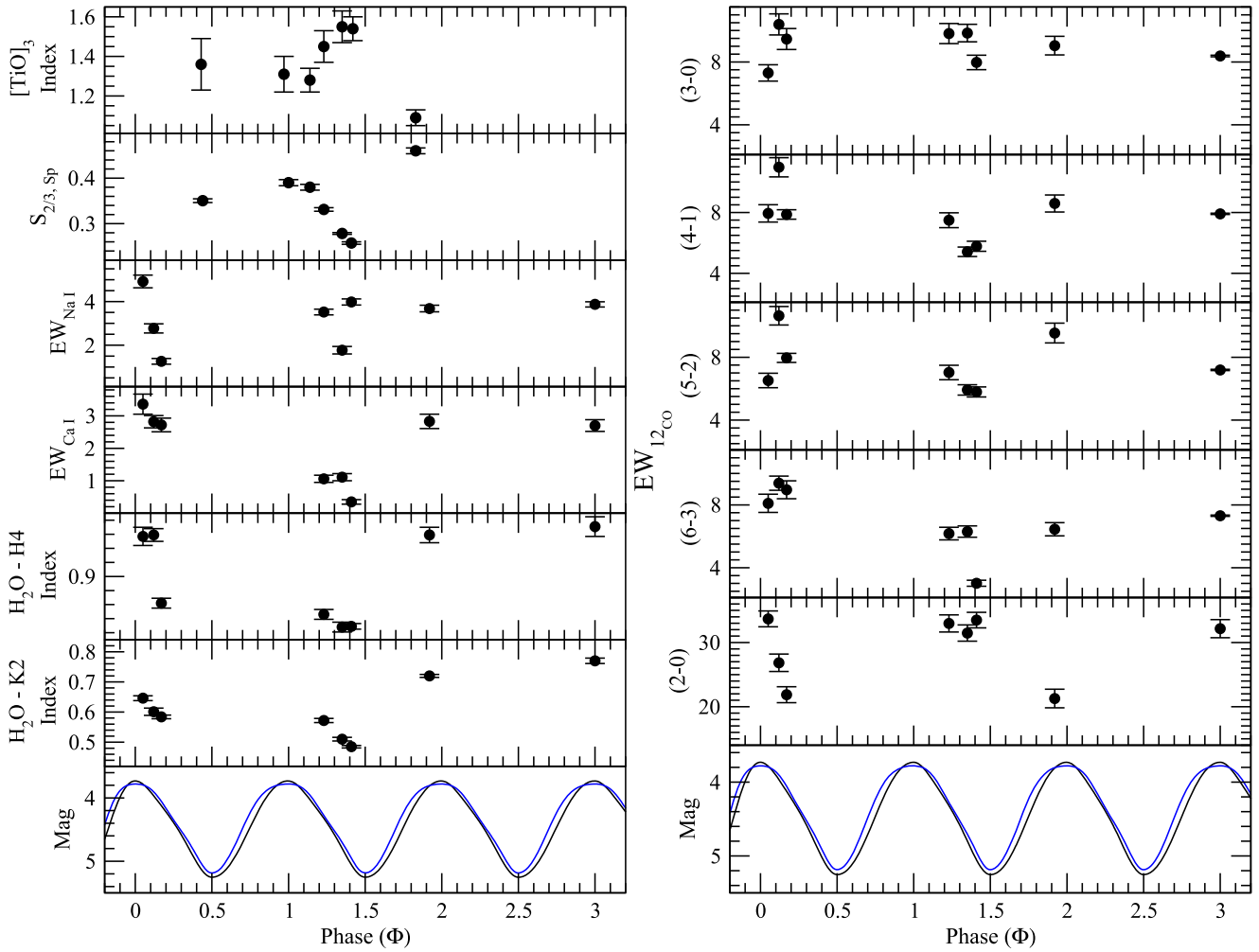

Figure 5. The phase variation of $[TiO]_3$, $S_{2/3,Sp}$, Na I, Ca I, H_2O-K2 equivalent width/index are shown with the visual phase. The bottom panel shows the K-light curve (black) and I-light curve (scaled with K-light curve).

Table 4
Definitions of Spectral Bands

Feature	Bandpass (μm)	Continuum Bandpass (μm)	References
$[TiO]_3$	0.8455–0.8725	0.8390–0.8410, 0.8700–0.8725	1
Na I	2.204–2.211	2.191–2.197, 2.213–2.217	2
Ca I	2.258–2.269	2.245–2.256, 2.270–2.272	2
^{12}CO(3–0)	1.5550–1.5625	...	2
^{12}CO(4–1)	1.5752–1.5812	...	2
^{12}CO(5–2)	1.5952–1.6020	...	2
^{12}CO(6–3)	1.6170–1.6220	...	2
^{12}CO(2–0)	2.289–2.302	2.270–2.272, 2.275–2.278 2.282–2.286, 2.288–2.289	2

Note. (1) Zhu et al. (1999), (2) Ramirez et al. (1997).

1.4, 1.9, and 2.7 μm in our spectral coverage (Rayner et al. 2009). It is clearly visible that the continuum shape is changing over the variability phases.

3.5.1. Phase-dependent Spectral Variability

The variation in the absorption depth of TiO and VO with $T_{\rm eff}$ has been well documented for some time (Merrill et al. 1962). Lockwood (1972) found that TiO band-strength indices decrease in stars later than M7, and they saturate in M9 Miras. We explore the phase variation of the $[TiO]_2$ index centered at 7100 Å as described in O'Connell (1973). However, the $[TiO]_2$ index shows no significant variation over the phase. Note that we do consider the optical phase variation here.

Another triple-headed absorption band of TiO at 8433, 8442, 8452 Å, $[TiO]_3$, is considered following Zhu et al. (1999) for such phase variation studies. The $[TiO]_3$ is defined as

$$[TiO]_3 = -2.5 \log\left(\frac{F_\lambda}{F_C}\right) \quad (4)$$

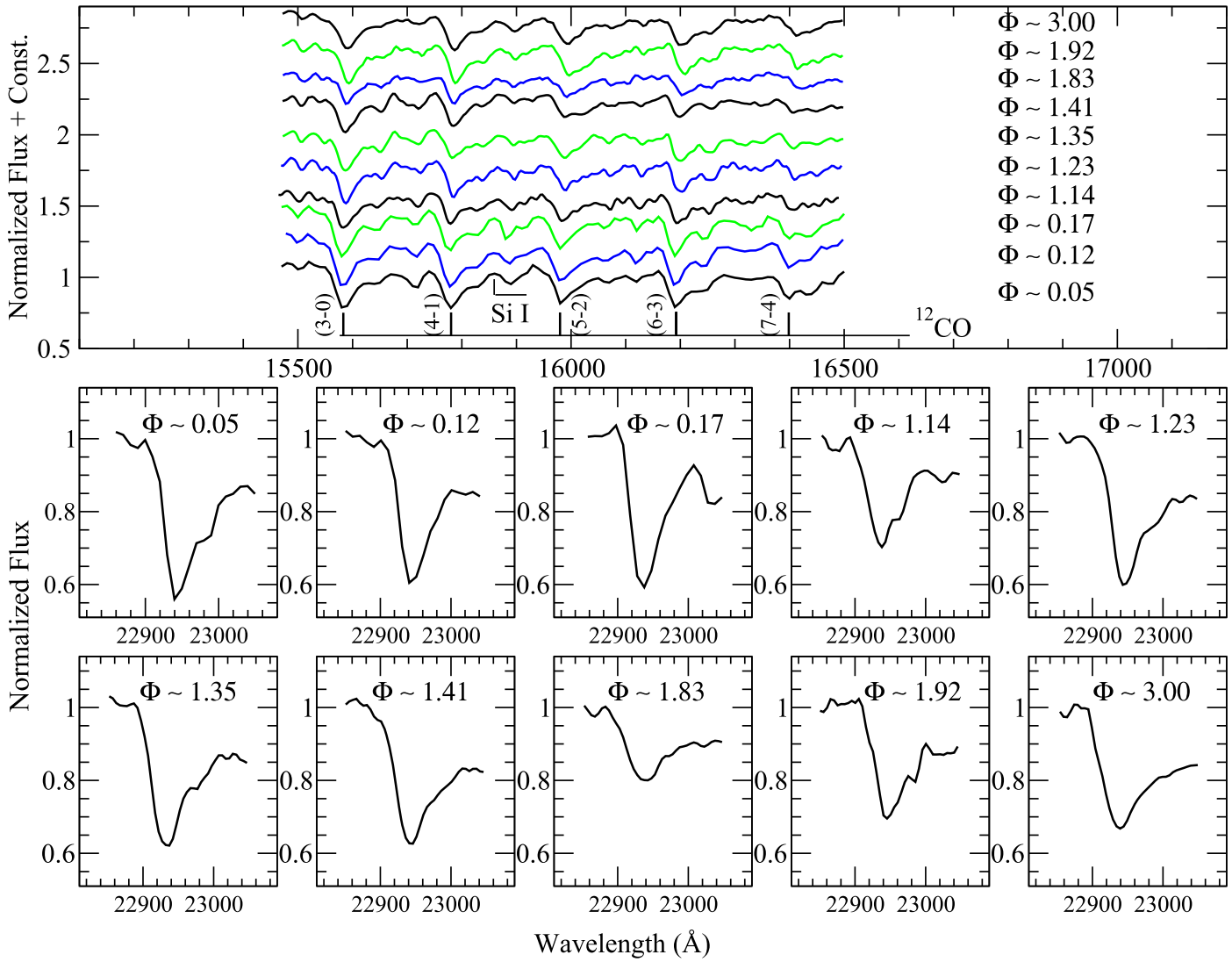

Figure 6. The changing shape of CO-second overtones and one CO first overtone at 2.29 μm with phases are shown here.

where, F_λ is the flux at λ, and F_C is the interpolated continuum at λ. The pseudo-continuum was generated in the left window of the band at 8390–8410 Å, and the right windows at 8700–8725 Å. Then, we normalized the spectrum by the continuum, and measured the $\frac{F_\lambda}{F_C}$ in the range 8455–8470 Å. As shown in Figure 5, the $[TiO]_3$ index shows significant variation with the pulsation phase; it increases as the visual brightness decreases, becomes constant at certain phases (saturation effect), and then further decreases with increasing visual brightness.

Figure 3 shows three strong absorption bands 706–724 nm (band1), 770–807 nm (band2), and 829–857 nm (band3), which are related to spectral types of static giants (Fluks et al. 1994). The flux ratio at different bands is defined by Fluks et al. (1994). We studied the flux ratio at those bands and found that the band2 to band3 ratio (as $S_{2/3,Sp}$) shows pronounced variation with phase, as is shown in Figure 5. The $S_{2/3,Sp}$ reaches its maximum at the visual maximum and reaches its minimum at the visual minimum.

We have measured the equivalent widths (EWs) for the atomic spectral Na I at 2.206 μm and Ca I at 2.263 μm. The continuum bands for Na I and Ca I are taken from Ramirez et al. (1997) and mentioned in Table 4. The spectra were normalized by the local pseudo-continuum, and EWs of the particular atomic features were estimated by using the splot task in the IRAF by fitting a Gaussian function to each feature. The Na doublet is present in the 2.2051–2.2099 μm region but blended with metallic lines like Si I (2.2069 μm), Sc I (2.2058 and 2.2071 μm), and V I (2.2097 μm) in our low-resolution spectra. The Ca triplet appears in the 2.2609–2.2665 μm regions and is very sensitive to temperature. The third and fourth panels of Figure 5 show their phase variation. The atomic lines, in particular, are weak features that are very difficult to measure in low-resolution spectra, and no significant trends with phase are apparent, except possibly for Ca.

In the 1.5–2.4 μm region, the first overtone ($\Delta\nu = 2$) and the CO-second overtone ($\Delta\nu = 3$) band heads of CO are the dominant features in the spectra as mentioned in the earlier section. We studied the phase-dependent variations of these 2–0 (first overtone) and 3–0, 4–1, 5–2, 6–3 (second overtone) ^{12}CO band heads. We estimated the EWs of CO at different phase considering the local continuum as mentioned in the Table 4. The continuum has been fitted with a first-order spline fitting function (linear interpolation) at peak points. We estimated the EWs of CO at different phases, as shown in

Table 5
Phase-dependent Study

Date of Obs.	Optical Phase	$[TiO]_3$ Index	$S_{2/3,Sp}$	Na I 2.20 μm	Ca I 2.26 μm	CO 3–0	CO 4–1	CO 5–2	CO 6–3	CO 2–0	H_2O-H4 Index	H_2O-K2 Index	Sp. Type[a]
2013 Mar 21.99	0.05	⋯	⋯	4.92 ± 0.29	3.36 ± 0.31	7.30 ± 0.52	7.94 ± 0.57	6.52 ± 0.46	8.1 ± 0.58	33.68 ± 1.23	0.96 ± 0.01	0.65 ± 0.01	⋯
2013 Apr 29.99	0.12	⋯	⋯	2.77 ± 0.21	2.82 ± 0.19	10.39 ± 0.67	10.97 ± 0.63	10.64 ± 0.59	9.38 ± 0.45	26.84 ± 1.36	0.96 ± 0.01	0.60 ± 0.01	⋯
2013 May 30.95	0.17	⋯	⋯	1.26 ± 0.13	2.72 ± 0.21	9.46 ± 0.67	7.87 ± 0.31	7.96 ± 0.29	8.96 ± 0.57	21.87 ± 1.24	0.86 ± 0.01	0.58 ± 0.01	⋯
2013 Oct 15.57	0.44	1.36 ± 0.13	0.350 ± 0.004	⋯	⋯	⋯	⋯	⋯	⋯	⋯	⋯	⋯	M9.5
2014 May 21.91	1.0	1.31 ± 0.09	0.390 ± 0.007	⋯	⋯	⋯	⋯	⋯	⋯	⋯	⋯	⋯	M9
2014 Aug 18.72	1.14	⋯	⋯	1.37 ± 0.11	1.10 ± 0.12	8.03 ± 0.44	6.02 ± 0.33	6.22 ± 0.34	6.023 ± 0.32	18.65 ± 1.08	0.90 ± 0.011	⋯	⋯
2014 Aug 19.83	1.14	1.28 ± 0.06	0.380 ± 0.006	⋯	⋯	⋯	⋯	⋯	⋯	⋯	⋯	⋯	M9
2014 Oct 06.73	1.23	1.45 ± 0.08	0.331 ± 0.003	3.52 ± 0.13	1.06 ± 0.11	9.81 ± 0.64	7.49 ± 0.49	7.03 ± 0.46	6.173 ± 0.40	32.97 ± 1.33	0.85 ± 0.01	0.57 ± 0.01	M9
2014 Dec 12.55	1.35	1.55 ± 0.08	0.278 ± 0.002	1.77 ± 0.17	1.11 ± 0.11	9.84 ± 0.56	5.42 ± 0.31	5.92 ± 0.33	6.30 ± 0.36	31.47 ± 1.27	0.83 ± 0.01	0.51 ± 0.01	M10
2015 Jan 13.58	1.41	⋯	⋯	3.98 ± 0.14	0.35 ± 0.07	7.97 ± 0.46	5.78 ± 0.33	5.788 ± 0.32	3.01 ± 0.19	33.49 ± 1.21	0.83 ± 0.01	0.48 ± 0.01	⋯
2015 Jan 18.56	1.41	1.54 ± 0.06	0.257 ± 0.003	⋯	⋯	⋯	⋯	⋯	⋯	⋯	⋯	⋯	M10
2015 July 05.79	1.83	1.09 ± 0.04	0.460 ± 0.006	1.94 ± 0.09	1.57 ± 0.17	6.85 ± 0.31	6.66 ± 0.30	6.03 ± 0.27	4.32 ± 0.20	19.52 ± 0.93	0.93 ± 0.01	⋯	M8.5
2015 Aug 11.88	1.92	⋯	⋯	3.68 ± 0.15	2.83 ± 0.22	9.04 ± 0.59	8.59 ± 0.56	9.54 ± 0.63	6.45 ± 0.42	21.27 ± 1.45	0.96 ± 0.01	0.72 ± 0.01	⋯
2016 Dec 19.54	3.00	⋯	⋯	3.87 ± 0.12	2.70 ± 0.18	8.38 ± 0.05	7.91 ± 0.04	7.19 ± 0.04	7.31 ± 0.04	32.15 ± 1.41	0.97 ± 0.01	0.77 ± 0.01	⋯

Note.
[a] The spectral type has been estimated using the correlation with $[TiO]_3$ Index.

Figure 5. The EWs of the 3–0 and 4–1 band heads does not demonstrate any significant change during the pulsation cycle. The EWs of the 2–0 first overtone band change significantly. The EWs of the 5–2 and 6–3 band heads showed weak variation. This result should be taken with caution, as such small variations might occur due to computational artifacts, continuum selection, and blending effects from the weak OH lines. The shock wave, in general, propagates through the Mira atmosphere (CO first overtone forming-layer) in between optical phase ∼0.1–0.2, which alters the velocity profile known from high-resolution spectra (Hinkle & Barnes 1979b; Nowotny et al. 2010). Even in our low- to intermediate-resolution spectra, the CO absorption features appear to change in Figure 6. It is expected that the combination of modified individual lines will also modify the shape of the band as a whole.

The shape of the NIR spectra in Miras is dominated by strong, broad water bands centered at the 1.4 μm, 1.9 μm, and 2.7 μm regions (Johnson et al. 1968). The depths of water bands vary with Mira phases and become strongest at minimum light (Strecker et al. 1978). Due to this water absorption, the *H*- and *K*-band spectra bend downward at the end of both bands. Thus, the curvature of the spectral changes depends on the water absorption. To quantify water absorption in our data, we measured the H_2O-H4 and H_2O-K2 indices, which show the curvature variation of the spectra. The H_2O-K2 index is taken from Rojas-Ayala et al. (2012) as

$$H_2O\text{-}K2 = \frac{\langle F(2.070\text{–}2.090)\rangle / \langle F(2.235\text{–}2.255)\rangle}{\langle F(2.235\text{–}2.255)\rangle / \langle F(2.360\text{–}2.380)\rangle}, \quad (5)$$

where $\langle F(a-b)\rangle$ represents the median flux level in the wavelength range defined by a and b in μm. Rojas-Ayala et al. (2012) calculated this index for M- and K-type dwarfs. Here, that same index is explored using the spectra for M-type giants in the wavelength range of 2.07–2.38 μm.

For the *H*-band spectra, several authors defined spectro-photometric indices to measure water absorption (e.g., Allers et al. 2007; Weights et al. 2009; Scholz et al. 2012). Here, we define a new H_2O-H4 index as,

$$H_2O\text{-}H4 = \frac{\langle F(1.531\text{–}1.541)\rangle / \langle F(1.670\text{–}1.690)\rangle}{\langle F(1.670\text{–}1.690)\rangle / \langle F(1.742\text{–}1.752)\rangle} \quad (6)$$

where $\langle F(a-b)\rangle$ represents the median flux level in the wavelength range defined by a and b in μm.

In Figure 5, the phase variation of these two H_2O-H4 and H_2O-K2 indices is shown. The smaller value of H_2O indices in *H* and *K* corresponds to greater amounts of H_2O opacity. The significant variations of these indices are apparent in Figure 5. In Figure 5, we see that the H_2O-H4 and H_2O-K2 indices show significant variation with the pulsation cycles, and the value of indices are strongest at visual maximum while weak at visual minimum, i.e., H_2O opacity is stronger at visual minimum. Our result confirms the trends already seen by Strecker et al. (1978).

3.5.2. Spectral Type

The depth of the triple-headed absorption band of TiO (8432, 8442, and 8452 Å) at the optical spectra is an excellent spectral-type indicator. Following Zhu et al. (1999), we estimate the spectral type (ST) of the object at a different variability phase, which is defined as the $[TiO]_3$ index ([TiO] at 8450 Å)

$$ST = 2.43 + 6.65[TiO]_3 - 1.12[TiO]_3^2. \quad (7)$$

We have measured the $[TiO]_3$ index using Equation (4) from the spectra as described in the earlier Section 3.5.1. The ST is estimated using the above relation in Equation (7), and the STs at different phases are shown the Table 5. The ST of the object varies from M8.5 to M10 over the phase of the pulsation cycle in our limited phase coverage. The saturation effect of $[TiO]_3$ is problematic to estimate the STs over phases, as described earlier in Section 3.5.1.

4. Summary and conclusion

From long-term optical/NIR photometric and spectroscopic observations, we have characterized the MASTER OT J2124 +32. Our main results are summarized as follows:

1. From the best-fits of optical/NIR light curves, we estimated the variability period of the object as 465 ± 30 days. The strong wavelength-dependent variability amplitudes in the optical to NIR wavelengths are observed as $\Delta I \sim 4$ mag, ΔC (400–900 nm) ∼3.4 mag, $\Delta J \sim 2.2$ mag, $\Delta H \sim 1.9$ mag and $\Delta K \sim 1.5$ mag. Such large periods and strong wavelength-dependent variability amplitude are seen in Miras only. Interestingly, a phase lag of ∼60 days between the optical and NIR light curves is also seen, like for Mira variables. Large $(J-K)$ NIR colors varying 1.78–3.0 mag over phases, signify that it is a red object, like cool Miras.
2. From the PL relation, the distance to the source is estimated to be 3.27 ± 0.02 kpc. The absolute bolometric magnitude is determined to be −5.29 ± 0.38 mag, corresponding to the luminosity of ∼10250 $L_\odot$.
3. Using DUSTY-based MoD code, we have completed the SED fit for NIR to far-IR data. The best-fit SED of all photometric measurements provides an effective temperature of 2800 K and dust shell temperature 1248 K. The SED provides a luminosity of the object of 9282 $L_\odot$, which is comparable to the P-L based estimation, and provides a mass-loss rate of $0.7 \times 10^{-6}\ M_\odot\ \mathrm{yr}^{-1}$.
4. From Optical/NIR spectra, we find that the source has many of the spectral signatures of a cool M-type star. The spectral features indicate it is an O-rich Mira, as it shows the most prominent features of VO band and TiO bands. We rule out an S- or C-type nature, as the ZrO bands at 1.03 and 1.06 μm and C_2 band-head at 1.77 μm are absent.
5. The phase-dependence of optical/NIR spectral features are studied. Notable variable features in all atomic and molecular lines (e.g., TiO, Ca I, H_2O, and CO bands) over phases are seen here, which are like commonly observed in Miras. Our optical spectral data show an apparent variation of the spectral type of the object over the pulsation cycle.

In conclusion, all of these observational properties of the object J2124+32 confirm that it is a new O-rich Mira variable toward Cygnus.

The authors are very much thankful to the anonymous referee for his/her critical and valuable comments, which helped us to improve the paper. This research work is

supported by the S N Bose National Centre for Basic Sciences under Department of Science and Technology, Govt. of India. The authors thank the staff of IAO, Hanle and CREST, Hosakote, who made these observations possible. The facilities at IAO and CREST are operated by the Indian Institute of Astrophysics, Bangalore. We acknowledge the usage of the TIFR Near Infrared Spectrometer and Imager (TIRSPEC). We also thank the staff of the Mt. Abu observatory, operated by the Physical Research Laboratory, Ahmedabad. S.G. is thankful to M. A. T. Groenewegen for helpful discussions and valuable suggestions on DUSTY code and MoD.

Software: starlink (Currie et al. 2014), IRAF (Tody 1986, Tody 1993), TIRSPEC pipe-line (Ninan et al. 2014), PERIOD044 (Lenz & Breger 2005), More of Dusty (MoD; Groenewegen 2012), DUSTY (Ivezić & Elitzur 1997), MARCS (Gustafsson et al. 2008)

ORCID iDs

Supriyo Ghosh https://orcid.org/0000-0003-4640-3369

References

Allers, K. N., Jaffe, D. T., Luhman, K. L., et al. 2007, ApJ, 657, 511
Alvarez, R., Jorissen, A., Plez, B., et al. 2000, A&A, 362, 655
Aringer, B., Girardi, L., Nowotny, W., et al. 2009, A&A, 503, 913
Bessell, M. S., Brett, J. M., Wood, P. R., & Scholz, M. 1989, A&A, 213, 209
Bessell, M. S., Castelli, F., & Plez, B. 1998, A&A, 333, 231
Bessell, M. S., Scholz, M., & Wood, P. R. 1996, A&A, 307, 481
Bieging, J. H., Rieke, M. J., & Rieke, G. H. 2002, A&A, 384, 965
Castelaz, M. W., & Luttermoser, D. G. 1997, AJ, 114, 1584
Castelaz, M. W., Luttermoser, D. G., Caton, D. B., & Piontek, R. A. 2000, AJ, 120, 2627
Cesetti, M., Pizzella, A., Ivanov, V. D., et al. 2013, A&A, 549, 129
Currie, M. J., Berry, D. S., Jenness, T., et al. 2014, ASPC, 485, 391
Cutri, R. M., Skrutskie, M. F., van Dyk, S., et al. 2003, yCat, 2246, 0
Cutri, R. M., Skrutskie, M. F., van Dyk, S., et al. 2013, yCat, 2328, 0
Dejonghe, H., & van Caelenberg, K. 1999, IAUS, 191, 501
Eggen, O. J. 1998, AJ, 115, 2435
Feast, M. W., Glass, I. S., Whitelock, P. A., & Catchpole, R. M. 1989, MNRAS, 241, 375
Fleischer, A. J., Gauger, A., & Sedlmayr, E. 1992, A&A, 266, 321
Fluks, M. A., Plez, B., The, P. S., et al. 1994, A&AS, 105, 311
Fox, M. W., & Wood, P. R. 1985, ApJ, 297, 455
Fox, M. W., Wood, P. R., & Dopita, M. A. 1984, ApJ, 286, 337
Gautschy-Loidl, R., Höfner, S., Jørgensen, U. G., & Hron, J. 2004, A&A, 422, 289
Groenewegen, M. A. T. 2012, A&A, 543, 36
Groenewegen, M. A. T., Lançon, A., & Marescaux, M. 2009, A&A, 504, 1031
Guha, N., Suklima, S., Angela, K., & Onaka, T. 2011, ApJ, 733, 93
Gustafsson, B., Edvardsson, B., Eriksson, K., et al. 2008, A&A, 486, 951
Habing, H. J. 1988, A&A, 200, 40
Habing, H. J. 1996, A&ARv, 7, 97
Hambsch, F.-J. 2012, JAVSO, 40, 1003
Herwig, F. 2005, ARA&A, 43, 435
Hinkle, K. H. 1978, ApJ, 220, 210
Hinkle, K. H., & Barnes, T. G. 1979a, ApJ, 227, 923
Hinkle, K. H., & Barnes, T. G. 1979b, ApJ, 234, 548
Hinkle, K. H., Hall, D. N. B., & Ridgway, S. T. 1982, ApJ, 252, 697
Hinkle, K. H., Wilson, T. D., Scharlach, W. W. G., & Fekel, F. C. 1989, AJ, 98, 1820
Höfner, S., Jørgensen, U. G., Loidl, R., & Aringer, B. 1998, A&A, 340, 497
Hughes, S. M. G., & Wood, P. R. 1990, AJ, 99, 784
Ireland, M. J., Scholz, M., & Wood, P. R. 2004, MNRAS, 352, 318
Ishihara, D., Onaka, T., Kataza, H., et al. 2010, A&A, 514A, 1
Ita, Y., & Matsunaga, N. 2011, MNRAS, 412, 2345
Ita, Y., Tanabé, T., Matsunaga, N., et al. 2004, MNRAS, 353, 705
Ivezić, Ž., & Elitzur, M. 1997, MNRAS, 287, 799
Ivezić, Ž., & Elitzur, M. 1999, arXiv:astro-ph/9910475
Johnson, H. L., Coleman, I., Mitchell, R. I., & Steinmetz, D. L. 1968, CoLPL, 7, 83
Jura, M., & Kleinmann, S. G. 1990, ApJ, 364, 663
Jura, M., & Kleinmann, S. G. 1992, ApJS, 79, 105
Jurić, M., Ivezić, Ž., Brooks, A., et al. 2008, ApJ, 673, 864
Keeley, D. A. 1970, ApJ, 161, 657
Kharchenko, N., Kilpio, E., Malkov, O., & Schilbach, E. 2002, A&A, 384, 925
Lançon, A., Hauschildt, P. H., Ladjal, D., & Mouhcine, M. 2007, A&A, 468, 205
Lançon, A., Mouhcine, M., Fioc, M., & Silva, D. 1999, A&A, 344, 21
Lançon, A., & Wood, P. R. 2000, A&AS, 146, 217
Le Bertre, T. 1992, A&AS, 94, 377
Lebzelter, Th., Hinkle, K. H., & Hron, J. 1999, A&A, 341, 224
Lenz, P., & Breger, M. 2005, CoAst, 146, 53
Lipunov, V., Gorbovskoy, E., Afanasiev, V., et al. 2016, A&A, 588, 90
Lipunov, V. M., Kornilov, V., Gorbovskoy, E., et al. 2017, MNRAS, 465, 3656
Lockwood, G. W. 1972, ApJS, 24, 375
Loidl, R., Höfner, S., Jørgensen, U. G., & Aringer, B. 1999, A&A, 342, 531
Lomb, N. R. 1976, Ap&SS, 39, 447
Mattei, J. A. 1997, JAVSO, 25, 57
Merrill, P. W., Deutsch, A. J., & Keenan, P. C. 1962, ApJ, 136, 21
Mondal, S., & Chandrasekhar, T. 2005, AJ, 130, 842
Mondal, S., Das, R. K., Ashok, N. M., et al. 2013, ATel, 4931, 1
Mondal, S., Lin, C. C., Chen, W. P., et al. 2010, AJ, 139, 2026
Ngeow, C.-C., Lucchini, S., Kanbur, S., Barrett, B., & Lin, B. 2013, arXiv:1309.4297
Ninan, J. P., Ojha, D. K., Ghosh, S. K., et al. 2014, JAI, 3, 1450006
Nowotny, W., Aringer, B., Höfner, S., Gautschy-Loidl, R., & Windsteig, W. 2005, A&A, 437, 273
Nowotny, W., Höfner, S., & Aringer, B. 2010, A&A, 514A, 35N
Nowotny, W., Lebzelter, T., Hron, J., & Höfner, S. 2005, A&A, 437, 285
O'Connell, R. W. 1973, AJ, 78, 1074
Olofsson, H. 2004, in Asymptotic Giant Branch Stars, ed. H. J. Habing & H. Olofsson (Berlin: Springer), 325
Perrin, G., Ridgway, S. T., Mennesson, B., et al. 2004, A&A, 426, 279
Ramirez, S. V., Depoy, D. L., Frogel, J. A., Sellgren, K., & Blum, R. D. 1997, AJ, 113, 1411
Rayner, J. T., Cushing, M. C., & Vacca, W. D. 2009, ApJS, 185, 289
Reid, M. J., & Goldston, J. E. 2002, ApJ, 568, 931
Rojas-Ayala, B., Covey, K. R., Muirhead, P. S., & Lloyd, J. P. 2012, ApJ, 748, 93R
Scargle, J. D. 1982, ApJ, 263, 835S
Schlafly, E. F., & Finkbeiner, D. P. 2011, ApJ, 737, 103
Schlegel, D. J., Finkbeiner, D. P., & Davis, M. 1998, ApJ, 500, 525
Scholz, A., Muzic, K., Geers, V., et al. 2012, ApJ, 744, 6
Smith, B. J., Leisawitz, D., Castelaz, M. W., & Luttermoser, D. 2002, AJ, 123, 948
Smith, B. J., Price, S. D., & Moffett, A. J. 2006, AJ, 131, 612
Soszyński, I., Udalski, A., Poleski, R., et al. 2012, AcA, 62, 219
Strecker, D. W., Erickson, E. F., & Witteborn, F. C. 1978, AJ, 83, 26
Tej, A., Lano¸n, A., & Scholz, M. 2003a, A&A, 401, 347
Tej, A., Lano¸n, A., Scholz, M., & Wood, P. R. 2003b, A&A, 412, 481
Thompson, R. R., Creech-Eakman, M. J., & van Belle, G. T. 2002, ApJ, 577, 447T
Tiurina, N., Lipunov, V., Gorbovskoy, E., et al. 2013, ATel, 4888, 1
Tody, D. 1986, Proc. SPIE, 627, 733
Tody, D. 1993, in ASP Conf. Ser. 52, ed. R. J. Hanisch, R. J. V. Brissenden, & J. Barnes (San Francisco, CA: ASP), 173
Tsuji, T. 2009, A&A, 504, 543
Wallace, L., & Hinkle, K. 1996, ApJS, 107, 312
Weights, D. J., Lucas, P. W., Roche, P. F., Pinfield, D. J., & Riddick, F. 2009, MNRAS, 392, 817
Whitelock, P., Marang, F., & Feast, M. 2000, MNRAS, 319, 728
Whitelock, P. A., Feast, M. W., & van Leeuwen, F. 2008, MNRAS, 386, 313W
Whitelock, P. A., Feast, M. W., van Loon, J. Th., & Zijlstra, A. A. 2003, MNRAS, 342, 86W
Winters, J. M., Fleischer, A. J., Le Bertre, T., & Sedlmayr, E. 1997, A&A, 326, 305
Winters, J. M., Le Bertre, T., Jeong, K. S., Helling, Ch., & Sedlmayr, E. 2000, A&A, 361, 641
Wittkowski, M., Boboltz, D. A., Driebe, T., et al. 2008, A&A, 479, 21
Wittkowski, M., Boboltz, D. A., Ohnaka, K., Driebe, T., & Scholz, M. 2007, A&A, 470, 191
Wood, P. R., Alcock, C., Allsman, R. A., et al. 1999, IAUS, 191, 151
Wood, P. R., & Sebo, K. M. 1996, MNRAS, 282, 958
Wright, N. J., Barlow, M. J., Greimel, R., et al. 2009, MNRAS, 400, 1413
Zhu, Z. X., Friedjung, M., Zhao, G., Hang, H. R., & Huang, C. C. 1999, A&AS, 140, 69